

Lawrence Berkeley National Laboratory

LBL Publications

Title

Using Nanoparticle X-ray Spectroscopy to Probe the Formation of Reactive Chemical Gradients in Diffusion-Limited Aerosols

Permalink

<https://escholarship.org/uc/item/3kz4f0pr>

Journal

The Journal of Physical Chemistry A, 123(28)

ISSN

1089-5639

Authors

Jacobs, Michael I

Xu, Bo

Kostko, Oleg

et al.

Publication Date

2019-07-18

DOI

10.1021/acs.jpca.9b04507

Peer reviewed

Using Nanoparticle X-ray Spectroscopy to Probe the Formation of Reactive Chemical Gradients in Diffusion-Limited Aerosols

Michael I. Jacobs,^{1,2} Bo Xu,² Oleg Kostko,² Aaron A. Wiegel,² Frances A. Houle,² Musahid Ahmed,² and Kevin R. Wilson^{2,*}

¹Department of Chemistry, University of California, Berkeley, CA, 94720, United States

²Chemical Sciences Division, Lawrence Berkeley National Laboratory, Berkeley, CA, 94720, United States

* Correspondence to: krwilson@lbl.gov, (510) 495-2474

Abstract:

For aerosol particles that exist in highly viscous, diffusion-limited states, steep chemical gradients are expected to form during photochemical aging in the atmosphere. Under these conditions species at the aerosol surface are more rapidly transformed than molecules residing in the particle interior. To examine the formation and evolution of chemical gradients at aerosol interfaces, the heterogeneous reaction of hydroxyl radicals (OH) on ~200-nm particles of pure squalane (a branched, liquid hydrocarbon) and octacosane (a linear, solid hydrocarbon), and binary mixtures of the two are used to understand how diffusion limitations and phase separation impact particle reactivity. Aerosol mass spectrometry is used to measure the effective heterogeneous OH uptake coefficient (γ_{eff}) and oxidation kinetics in the bulk, which are compared with the elemental composition of the surface obtained using X-ray photoemission. When diffusion rates are fast relative to the reaction frequency, as is the case for squalane and low viscosity squalane-octacosane mixtures, the reaction is efficient ($\gamma_{eff} \sim 0.3$) and only limited by the arrival of OH to the interface. However, for cases where the diffusion rates are slower than reaction rates, as in pure octacosane and higher viscosity squalane-octacosane mixtures, the heterogeneous reaction occurs in a mixing-limited regime and is ~10x slower ($\gamma_{eff} \sim 0.03$). This is in contrast to carbon and oxygen K edge X-ray absorption measurements that show that the octacosane interface is oxidized much more rapidly than that of pure squalane particles. The O:C ratio of the surface (estimated to be the top 6-8 nm of the interface) is measured to change with a rate constant of $(3.0 \pm 0.9) \times 10^{-13}$ and $(8.6 \pm 1.2) \times 10^{-13}$ cm³ molecule⁻¹ s⁻¹ for squalane and octacosane particles, respectively. The differences in surface oxidation rates are analyzed using a previously published reaction diffusion model, which suggests that a 1-2 nm highly oxidized crust forms on octacosane particles, whereas in pure squalane the reaction products are homogeneously mixed within the aerosol. This work illustrates how diffusion limitations can form particles with highly oxidized surfaces even at relatively low oxidant exposures, which is in turn expected to influence their microphysics in the atmosphere.

41 **I. Introduction:**

42 Recent work provides evidence that atmospheric aerosol particles exist in solid, liquid and
43 highly viscous, diffusion-limited phase states, with viscosities ranging from $<10^2$ to $>10^8$ Pa s.¹⁻⁴
44 Atmospheric aerosol are transformed by photochemical reactions, heterogeneous oxidation and
45 condensation of low-volatility organic species to yield increasingly oxidized, less volatile and
46 more hygroscopic particles.⁵ Chemical gradients are expected to form in semisolid, highly viscous
47 particles as they age in the atmosphere leading to more rapid changes in surface composition and
48 potentially affecting their atmospheric fates. For example, rapidly changing the chemical nature of
49 the aerosol surface could influence its ability to act as a cloud condensation nucleus.⁶⁻⁹ Because
50 steep chemical gradients in aerosol could change its chemistry with atmospheric trace gases, it is
51 important to understand the formation of chemical gradients and the chemical nature of the
52 interface.

53 The viscosity and the phase-state of an aerosol particle or a film has been measured to have
54 a significant effect on heterogeneous oxidation kinetics.¹⁰⁻²¹ Many species can exist as amorphous
55 semisolids or glasses with very slow internal diffusion at low relative humidity or low temperature,
56 which has been observed to slow heterogeneous oxidation kinetics.^{10,11,14-18} For example,
57 heterogeneous oxidation kinetics of levoglucosan were found to slow with decreasing relative
58 humidity, which decreased diffusoreactive lengths.¹¹ Additionally, a study found the effective
59 uptake coefficient of squalane ($C_{30}H_{62}$, a branched hydrocarbon that is liquid at room temperature)
60 to be significantly larger than octacosane ($C_{28}H_{58}$, a linear hydrocarbon that is solid at room
61 temperature) even though the individual molecules were estimated to have similar reactivity with
62 the OH radical.¹⁹ The product distribution was also different for squalane and octacosane. While
63 squalane showed functionalization throughout the molecule, octacosane was only functionalized

64 at the ends of the molecules. This suggested that while squalane was free to diffuse and rotate in
65 the particle, octacosane molecules experienced “surface freezing”, wherein the linear alkane chains
66 preferentially orient normal to the surface.^{19,22} Because the OH radical reacts at the top ~1 nm in
67 organic aerosol,²³ the differences in effective uptake coefficients were attributed to differences in
68 phase state and the ability for molecules to diffuse to the interface to react.

69 Recent modeling results have focused on how diffusion limitations can lead to emergent
70 properties of aerosol particles.^{16,24–27} The overall reactivity of an aerosol particle to heterogeneous
71 oxidation is a balance between the flux of oxidant at the surface and the internal mixing dynamics.
72 To understand reactivity across a broad range of diffusion coefficients, a reaction-diffusion index
73 (I_{RD}), also known as the Damköhler number, has been defined by Houle et al. to be^{25,26}

$$74 \quad I_{RD} = k_{rx}[gas]\tau_{cd}, \quad (1)$$

75 where k_{rx} is the rate constant for reaction between gas phase oxidant and species in the particle,
76 $[gas]$ is the concentration of gas phase oxidant, and τ_{cd} is the characteristic mixing time, which is
77 proportional to the square of the particle diameter and inversely proportional to the molecular
78 diffusion coefficient. If $I_{RD} \ll 1$, then mixing is fast relative to the arrival of the gas phase oxidant
79 to the aerosol surface and the supply of OH limits the reaction. If $I_{RD} \gg 1$, then the internal mixing
80 rate to refresh molecules at the aerosol surface is rate limiting. Thus, even though the reactive
81 uptake coefficient of a particle may be constant, changes in its bulk composition and the measured
82 effective uptake coefficient will depend upon the exact experimental timescales (i.e. laboratory vs.
83 atmosphere). At larger I_{RD} , bulk composition changes much more slowly, and large chemical
84 gradients form within the particle as the surface becomes more highly oxidized than the bulk.^{14,18}
85 For this study, two extremes of I_{RD} are examined. To do this two structurally related molecules are
86 selected with similar OH reactivity, but with mixing times that are orders of magnitude different.

87 The techniques that are commonly used to study aerosols—such as aerosol mass
88 spectrometry,²⁸ scanning transmission X-ray microscopy,²⁹ scanning electron microscopy,³⁰ and
89 chromatographic methods coupled with mass spectrometry³¹—probe volume-weighted aerosol
90 chemistry. These techniques measure average bulk composition or micron-scale heterogeneity, but
91 are unable to detect nano-scale spatial heterogeneity that is expected to form in diffusion-
92 limited aerosol particles. By reacting coated aerosols, there has been some work to determine how
93 spatial heterogeneity can affect oxidation kinetics.³² There has also been work to develop
94 analytical techniques that are more surface sensitive and can measure spatial heterogeneity within
95 aerosol particles. For example, depth profiling of aerosol particles was achieved by introducing a
96 particle stream into a heated gas stream and only ionizing/detecting the gas-phase species that
97 evaporated from the particle surface.^{14,33–35} Additionally, surface sensitivity has been achieved by
98 using extractive electrospray ionization to desorb and ionize molecular species from the aerosol
99 interface.^{36,37} Surface-sensitivity has also been achieved using nonlinear spectroscopic techniques,
100 such as second harmonic scattering from free aerosol particles³⁸ or sum frequency generation from
101 aerosol collected onto a filter substrate.^{39,40} However, there are few online, universally surface
102 sensitive measurements that can measure the formation and dissipation of chemical gradients
103 within a particle *in situ*.

104 Photoemission spectroscopy is a universally surface sensitive measurement because of the
105 short electron attenuation length (EAL) in materials. The study of photoemission from free aerosol
106 particles is still in its infancy.⁴¹ Several experiments have used ultraviolet photoelectron
107 spectroscopy (UPS) to study the electronic structure of free nanoparticles.^{42–53} Many of these
108 studies have used a velocity map imaging spectrometer to image a projection of the nascent
109 photoelectron distribution of low energy electrons that originated from valence energy

110 levels.^{42,43,46-53} Additionally, X-ray photoelectron spectroscopy (XPS) studies have probed free
111 nanoparticles to provide elemental information of the surface.^{51,54-62} Photoemission
112 spectroscopy—UPS, XPS and X-ray absorption spectroscopy (XAS)—has previously been used
113 to study the surfaces of liquid squalene aerosol particles during a surface reaction with ozone.⁵¹
114 However, photoemission spectroscopy has not been used to study heterogeneous chemistry in
115 particles with diffusion limitations, wherein the reaction is expected to exhibit substantial spatial
116 heterogeneity.

117 The heterogeneous oxidation of triacontane ($C_{30}H_{62}$, a linear hydrocarbon) has been
118 previously studied using an aerosol mass spectrometer to probe changes in bulk composition.^{63,64}
119 Using a reaction-diffusion kinetic model, it was predicted that under laboratory conditions the
120 surface of the particle was oxidized much more rapidly than the bulk (i.e. $I_{RD} \gg 1$).⁶⁴ Here,
121 photoemission is used to probe the surface reaction of OH on squalane and octacosane particles,
122 which represent two limiting cases for studying the formation of chemical gradients: $I_{RD} \ll 1$
123 (squalane) and $I_{RD} \gg 1$ (octacosane).

124 **II. Experimental Methods:**

125 The experimental setup used to study OH radical heterogeneous chemistry was nearly
126 identical to that described previously^{51,65} and is shown in Figure 1. Briefly, particles are generated
127 by flowing nitrogen through a heated reservoir containing either squalane, octacosane or a mixture
128 of the two (molecular structures are shown in Figure 1b and 1c). After the oven, particles pass
129 through an additional length of heated tubing (~ 80 °C) for annealing in an effort to make the
130 particles more spherical. The particle flow was mixed with oxygen (10%), humidified nitrogen
131 (30%), dry nitrogen, ozone, and a gas-phase OH tracer (~ 0.5 ppm acetone). The total flow rate was
132 ~ 1000 sccm. The particle concentrations were typically $\sim 1 \times 10^6$ and $5-10 \times 10^6$ particles/cm³ for

133 mass spectrometry and photoemission measurements, respectively. The flow was introduced into
134 a quartz flow tube (2.5 cm inner diameter, 140 cm length). Particles had an average residence time
135 of ~37 s in the flow tube. The particles were oxidized by the OH radical, generated within the flow
136 tube by the photolysis of ozone in the presence of water vapor using mercury lamps at 254 nm.
137 After the flow tube, the concentration of the gas-phase tracer was measured using a gas
138 chromatograph (GC). From the decay of acetone and its OH reaction rate constant ($k_{\text{acetone}} = 1.8 \times$
139 $10^{-13} \text{ cm}^3 \text{ molecule}^{-1} \text{ s}^{-1}$),⁶⁶ the OH exposure ($\langle \text{OH} \rangle_t \cdot t$) was calculated. A scanning mobility particle
140 sizer (SMPS) after the flow tube quantified changes in the particle size distribution with oxidation.

141 The bulk chemical composition of the aerosol was measured using a vacuum ultraviolet
142 aerosol mass spectrometer (VUV-AMS).⁶⁷ The particles were collimated using an aerodynamic
143 lens (ADL) and vaporized on a 135 °C heated block. The resulting vapor was ionized using 10.2
144 eV photons from the Chemical Dynamics Beamline (9.0.2) at the Advanced Light Source (ALS)
145 at Lawrence Berkeley National Laboratory. The effective uptake coefficient of particles comprised
146 of pure squalane, pure octacosane and mixtures of the two were determined as previously
147 described.⁶⁵ Details are provided in the Supporting Information.

148 The aerosol surface composition was probed by XPS and XAS. Specifically, XPS was used
149 to study the heterogeneous oxidation of pure squalane particles by the OH radical, and XAS at the
150 carbon and oxygen K edges was used to study the heterogeneous oxidation of pure squalane and
151 octacosane particles. The details of these measurements have been described previously.^{51,60}
152 Briefly, particles were introduced into a velocity map imaging (VMI) spectrometer via an ADL
153 and photoelectrons were mapped onto a multichannel plate (MCP)/phosphor detector.⁶⁰ C1s XPS
154 spectra were obtained using a photon energy of 330 eV. Particle and background images were
155 collected for 300 s, and a photoelectron spectrum from the background-subtracted images were

156 obtained using conventional techniques.⁶⁸ XAS spectra were collected by scanning the incident
157 photon energy and measuring the intensity of low kinetic energy (KE), secondary electrons (KE
158 <10 eV) that are generated by inelastic scattering of Auger electrons. A photomultiplier tube was
159 used to measure the total electron yield (TEY) from the MCP-phosphor detector. Carbon and
160 oxygen K edge XAS spectra were collected from 280-300 eV and 526-552 eV, respectively. The
161 spectra were collected with 0.2 eV steps and exposure times of 1 s per step. X-ray measurements
162 were done at beamline 6.0.2 at the ALS.

163 **III. Results and Discussion:**

164 **a) Bulk squalane and octacosane particle measurements.** Aerosol mass spectra of pure squalane
165 and octacosane are shown in Figures 2a and 2b, respectively. The mass spectra of squalane and
166 octacosane have molecular ions at m/z 422 and 394, respectively. As the particles react with OH,
167 the intensities of the molecular ions decrease. While surface freezing of octacosane drives the
168 chemistry through aldehydes, the same peroxy radical chemistries are expected to occur in
169 squalane and octacosane (shown in Figure S1 of the Supporting Information).^{19,25,64} After H-atom
170 abstraction by OH, peroxy radicals are formed via O_2 addition to an alkyl radical. The subsequent
171 reaction pathways of peroxy radicals typically form carbonyl and alcohol functional groups.
172 Figure 2c shows the mass spectrum of squalane after about half of the initial concentration of
173 squalane reacted (OH exposure is 5.3×10^{11} molecule s cm^{-3}). As the particles were heterogeneously
174 oxidized by the OH radical, oxygenated products were detected and are consistent with previous
175 observations.^{65,69,70}

176 Figure 2d shows the mass spectrum of octacosane after about half of its initial
177 concentration is consumed (OH exposure is 4.0×10^{12} molecule s cm^{-3}). Octacosane reacts much
178 more slowly than squalane (i.e. a much higher OH exposure is required to consume half of the

179 octacosane). In addition, no functionalized products from heterogeneous oxidation are observed in
180 the mass spectrum. This is consistent with previous observations, wherein the quantity of reaction
181 products from octacosane after ~ 1 oxidation lifetime were substantially less intense than those
182 observed from squalane oxidation.¹⁹ In this previous study, only the ends of the octacosane
183 molecules reacted, suggesting that surface alignment and diffusion limitations allowed only the
184 small number of molecules at the interface to react with OH. Thus, because the number of
185 molecules at the interface is small relative to the bulk, and the products are expected to be highly
186 oxidized (which makes them more difficult to observe using the bulk sensitivity of the VUV
187 photoionization technique), it is possible the measurement here is not sensitive enough to observe
188 the reaction products of octacosane.

189 The decay of the molecular ions at different OH exposures were monitored, and the
190 effective uptake coefficients of pure squalane and octacosane were determined to be 0.31 ± 0.06
191 and 0.03 ± 0.01 , respectively. The uptake coefficient for squalane is very similar to previous
192 measurements.^{19,65,71-73} Ruehl *et al.* previously measured an effective uptake coefficient of
193 0.18 ± 0.11 for octacosane,¹⁹ and Richards-Henderson *et al.* previously measured an effective
194 uptake coefficient of ~ 0.17 for triacontane.^{72,73} Both of these measurements are larger than the
195 value measured here. Since solid n-alkane particles form needle-like morphologies,⁷⁴ an annealing
196 oven was used to melt the particles to make them more spherical, which helped with aerodynamic
197 focusing in the spectrometer. Non-spherical particles have a larger surface area, which leads to
198 larger OH collision frequencies and faster heterogeneous reaction rates. Because Ruehl *et al.* and
199 Richards-Henderson *et al.* did not anneal the solid n-alkane particles, differences in particle
200 morphology (i.e. surface area) could explain the larger effective uptake coefficients reported in
201 their work.

202 Given the distribution of abstractable H atoms in each molecule, the gas-phase reactivities
203 of squalane and octacosane were estimated to be very similar ($k_{gas} = 4.0 \times 10^{-10}$ and 3.7×10^{-10} cm³
204 molecule⁻¹ s⁻¹, for squalane and octacosane, respectively).⁷⁵ Because particle size and OH
205 concentration were similar for both experiments, differences in internal mixing times likely explain
206 the large differences in effective uptake coefficient.²⁴ The self-diffusion coefficients in squalane⁷⁶
207 and triacontane⁶⁴ (a linear hydrocarbon very similar to octacosane) are 7×10^{-7} and 8.3×10^{-19} cm² s⁻¹,
208 respectively. Thus, 200-nm aerosols comprised of squalane and octacosane will have
209 characteristic mixing times of $\sim 10^{-5}$ and $\sim 10^7$ s, respectively. Based on the present reaction
210 conditions, squalane and octacosane have I_{RD} of $\sim 10^{-7}$ and $\sim 10^5$, respectively, suggesting that these
211 particles react in much different rate limiting regimes (i.e. OH flux limited vs. diffusion
212 limited).^{25,26}

213 Figure 3 shows the effective uptake coefficients of octacosane and squalane measured in
214 different squalane-octacosane mixtures. As the squalane mole fraction (x_{sqa}) increases, the
215 octacosane molecular ion is observed to decay faster (Figure 3a). Figure 3b shows the computed
216 effective uptake coefficients for octacosane and squalane as a function of x_{sqa} . At higher
217 concentrations of squalane ($x_{sqa} > 0.8$), the effective uptake coefficient of both octacosane and
218 squalane are nearly identical to pure squalane, suggesting that diffusion is fast relative to reaction
219 frequency (i.e. $I_{RD} \ll 1$ and that the reactions occur in an OH flux limited regime). This is consistent
220 with the two molecules having similar estimated reactivity towards OH, and the particles existing
221 as a well-mixed liquid on the timescale of the heterogeneous reaction frequency.

222 As the concentration of squalane decreases ($0.6 < x_{sqa} < 0.8$), the particle becomes more
223 viscous and the effective uptake coefficients of both octacosane and squalane decrease. At these
224 compositions, the viscosity in the particle increases, such that diffusion is slow relative to the

225 reaction frequency. The decrease in measured effective uptake suggests that the particle is
226 transitioning from an OH flux limited to a bulk diffusion limited regime. In this transitory regime,
227 the molecules in the aerosol interior become more inaccessible for reaction at the interface. As
228 diffusion continues to slow within the particle, ultimately only the molecules that reside within the
229 reacto-diffusive length of OH (1-2 nm) react heterogeneously.²³ The heterogeneous oxidation of
230 citric acid at different RHs showed a similar effect.¹⁴ At high RH, the viscosity of the citric acid
231 particle was low and the particle could mix freely (i.e. the reacto-diffusive length was larger than
232 the radius of the particle and $I_{RD} \ll 1$). At lower RH, the viscosity decreased, and both the measured
233 effective uptake coefficient and the reacto-diffusive length were smaller (i.e. $I_{RD} > 1$).

234 When the initial squalane composition decreases further ($x_{\text{sqa}} < 0.6$), the squalane and
235 octacosane effective uptake coefficients diverge and approach the values measured in their pure
236 states. The differences in the behavior of the molecular components suggests that at these mole
237 fractions, the particles do not exist as homogeneous mixture, but rather are phase separated. Phase
238 separation has been previously observed in particles composed of mixtures of solid and liquid
239 components (such as mixtures of oleic acid and stearic acid).⁷⁴ Thus, by changing the composition
240 of the particle, heterogeneous oxidation is observed to occur in either an OH flux limited (liquid
241 well-mixed particles), organic mixing limited (semi-solid, viscous particles) or phase separated.

242 **b) X-ray photoelectron spectroscopy of squalane particles.** X-ray photoelectron spectroscopy
243 can measure average O:C (oxygen-to-carbon) ratios by directly probing the chemical composition
244 of the surface.^{51,77} XPS spectra from the heterogeneous oxidation of squalane particles are shown
245 in Figure 4. The spectra were collected with 330 eV photons (resulting in ~ 40 eV KE
246 photoelectrons). An XPS spectrum of unoxidized squalane particles is shown in Figure 4a, and for
247 comparison an XPS spectrum of squalane oxidized at an OH exposure of 3.8×10^{12} molecule s cm^{-2}

248 ³ is shown in Figure 4b. The spectrum of oxidized squalane has a broad shoulder at higher binding
249 energies, which is attributed to the formation of reaction products containing new oxygenated
250 functional groups.

251 To extract a quantitative measure of the chemical composition of the surface of the particle,
252 the XPS spectra were fit using a method adapted from previous studies.^{51,77} Since pure squalane is
253 composed of only one type of carbon (methylene carbon, CH_x), a single Gaussian peak (FWHM
254 = 2.0 eV) was first fit to the unoxidized squalane spectrum. Next, the most highly oxidized
255 squalane spectrum was fit using two Gaussian peaks: the CH_x peak (which had the same
256 parameters as in the unoxidized squalane spectrum) and an oxygenated carbon peak, C_{ox} (which
257 was constrained to have the same FWHM as the CH_x peak). The C_{ox} peak was shifted by 2.0 eV
258 relative to methylene CH_x peak, which is in good agreement with the average shift expected for
259 carbonyls and alcohols.⁷⁸ The same two peaks were fit to the squalane spectra at each OH exposure.
260 Based on the expected reaction products and the relative shift of the C_{ox} peak, only one oxygen
261 atom is associated with each C_{ox} (i.e. only ketones and alcohols were formed).^{65,79} Thus, by
262 monitoring the relative intensity of the C_{ox} peak, the O:C ratio at the surface could be measured
263 directly (Figure 4c). The experimental O:C ratios are in good agreement with the bulk O:C ratios
264 measured with an AMS from a previous study (shown as the red line in Figure 4c).⁷⁰

265 The O:C ratios measured with XPS were used to inform the X-ray absorption
266 measurements as described below. Unfortunately, we were unable to measure XPS spectra from
267 octacosane particles. Even with annealing, it is suspected that the octacosane particles were not
268 completely spherical and poorly collimated by the aerodynamic lens, leading to poor transmission
269 efficiency and low XPS signal-to-noise ratio in the apparatus.

270 **c) X-ray absorption of squalane and octacosane particles.** XAS spectra at the carbon and
271 oxygen K edges were collected by scanning the incident photon energy and measuring the intensity
272 of low KE secondary electrons. An example distribution of low KE electrons from organic aerosol
273 has been previously reported,^{51,60} and is peaked around ~3 eV kinetic energy. Thus, based upon
274 previous studies of the electron attenuation length in organic nanoparticles, the XAS measurements
275 are expected to probe the topmost ~3-4 nm of the particle interface,⁵² as will be discussed in more
276 detail below.

277 Figure 5 shows the carbon K edge XAS spectra of squalane and octacosane at different OH
278 exposures. The spectra were area normalized using the TEY signal from 284 to 300 eV. For both
279 particles, at higher OH exposures, a pre-edge feature at ~286 eV grows in, and the intensity at the
280 initial pre-edge feature (~287 eV) decreases and blue shifts. The appearance of the pre-edge feature
281 arises due to an increasing number of different functional groups at the particle surface.⁸⁰ Based
282 on the reaction mechanism (Supporting Information, Figure S1), alcohols and carbonyls are likely
283 contributors to this pre-edge feature for squalane (low I_{RD}), and carbonyls and carboxylic acids are
284 likely contributors to this pre-edge feature for octacosane (high I_{RD}).²⁵ As shown by a comparison
285 of gas-phase carbon K edge XAS spectra of ethane, ethanol, acetaldehyde and acetic acid, the $1s$
286 $C(CO) \rightarrow \pi^*$ transition of carbonyls is the most likely assignment for this pre-edge spectral feature
287 (Supporting Information, Figure S2).⁸¹ However, without XAS calculations, it is difficult to
288 determine precisely which chemical species are responsible for all of the spectral changes
289 observed.

290 Both the squalane and octacosane carbon K edge XAS spectra exhibit an isosbestic point
291 at ~286.5 eV, indicating that there are at least two distinct populations of species that evolve during
292 the reaction. Oxidation kinetics were extracted from the spectra by calculating the ratio of the

293 spectral area to the left and right of the isosbestic point as a function of OH exposure (Figure 5c).
294 This method calculates the relative intensity of the pre-edge feature, which is assumed to be
295 proportional to oxygenated products at the surface. As shown in Figure 5c, the pre-edge feature
296 grows much more rapidly for octacosane than for squalane. A rate constant (k) describing the
297 growth of a signal with increased oxidation was calculated using:

$$298 \quad I_t = I_{max}(1 - e^{-k(OH)_t \cdot t}), \quad (2)$$

299 where I_t and I_{max} are the signal intensity at a given OH exposure and the maximum possible signal
300 intensity, respectively. The phenomenological rate constants for squalane and octacosane that best
301 describe the kinetic rise of this pre-edge feature are $(3.2 \pm 1.0) \times 10^{-13}$ and $(9.0 \pm 1.0) \times 10^{-13}$ cm³
302 molecule⁻¹ s⁻¹, respectively. Since the starting diameter of squalane and octacosane were similar,
303 both measured to be $\sim 200 \pm 40$ nm, these heterogeneous rate constants can be directly compared.
304 Thus, even though squalane appears much more reactive when observed with bulk sensitive
305 probes, the surface of octacosane oxidizes ~ 3 x faster. This measurement suggests that a chemical
306 gradient forms during the oxidation of octacosane. However, because X-ray absorption at the
307 carbon K edge probes the bonding environment around carbon atoms and changing speciation
308 affects the shape of the spectrum, the magnitude of the chemical gradient cannot be determined by
309 these data alone. Thus, direct probes of oxygenated species (such as oxygen K edge XAS) are
310 necessary to quantify the absolute magnitudes of chemical gradients.

311 Figure 6 shows the oxygen K edge XAS spectra of squalane and octacosane as a function
312 of OH exposure. The spectra are normalized to the intensity between 526-528 eV, which arises
313 from the tailing edge of the carbon K edge absorption. Because of the short EAL of low KE
314 photoelectrons, the pre-edge intensity has previously been reported to be proportional to particle
315 surface area (as measured by the SMPS).⁵¹ Similar to the oxygen K edge XAS spectra observed

316 during squalene ozonolysis, two peaks are observed to grow in with increasing OH exposure.⁵¹
317 The peak at ~532 eV is slightly red-shifted in octacosane compared to squalane. The reason for
318 this shift is unclear. It could arise from different molecular species (which are predicted to arise
319 from differences in particle diffusion rates)²⁵ or from differences in intermolecular bonding, since
320 XAS probes unoccupied molecular orbitals and Rydberg states that are very diffuse and sensitive
321 to the bonding environment.

322 Because the oxygen K edge XAS spectra were normalized by scaling each spectrum by the
323 pre-edge intensity (526-528 eV)—which arises from extended carbon K edge absorption—the
324 intensities in the spectra are directly proportional to the O:C ratios at the surface. The calibration
325 factor to relate XAS intensity to O:C ratio was determined using data from both squalene
326 ozonolysis and squalane oxidation. The change in the O:C ratio with increasing squalene
327 ozonolysis was directly measured using XPS. The measured O:C ratio was related to the peak
328 intensities in the oxygen K edge XAS spectra.⁵¹ In this work, XPS was used to directly measure
329 the O:C ratio of squalane particles as they were oxidized. Using this XPS data, the O:C ratio at
330 each OH exposure shown in Figure 6a was determined. Plotting the O:C ratio as a function of
331 oxygen K edge XAS peak intensity for both squalene ozonolysis and squalane oxidation yields a
332 linear relationship (Supporting Information, Figure S3). Thus, using this linear relationship
333 between oxygen XAS intensity and O:C ratio, we can obtain the chemical composition of the
334 surface of squalane and octacosane particles with increasing heterogeneous oxidation.

335 The change in the O:C ratio for squalane and octacosane is shown in Figure 7a. Using Eq.
336 2, the rate constants for the change in O:C ratio at the surfaces of squalane and octacosane are
337 $(3.0 \pm 0.9) \times 10^{-13}$ and $(8.6 \pm 1.2) \times 10^{-13}$ cm³ molecule⁻¹ s⁻¹, respectively. As with the carbon K edge
338 XAS spectra, even though the bulk composition of octacosane changes ~10x more slowly than

339 that of squalane, the surface O:C ratio increases $\sim 3x$ faster. These rate constants are in good
340 agreement with those describing the spectral changes in the carbon K edge XAS spectra shown in
341 Figure 5, which is a good internal check of our spectra analysis approach.

342 To directly compare the growth of the surface O:C ratio in the two particles, OH exposure
343 was converted to bulk oxidation lifetimes using the effective uptake coefficient of squalane and
344 octacosane from the AMS measurements. A bulk oxidation lifetime is the number of reactive OH
345 collisions divided by the total number of molecules in the particle. From the second order reaction
346 rate constant (k_1) describing the decay of the molecular ion, the number of lifetimes is,

$$347 \quad \text{lifetimes} = k_1 \langle \text{OH} \rangle_t \cdot t. \quad (3)$$

348 Figure 7b shows that over the range of OH exposures measured here, the squalane reacts up to ~ 4
349 lifetimes, while octacosane only up to ~ 0.5 lifetime. By plotting the O:C ratio measured with
350 photoemission as a function of bulk oxidation lifetime, the change in the surface composition is
351 related to the change in the bulk composition. The dashed red line in Figure 7b shows the predicted
352 bulk O:C ratio as a function of OH exposure for squalane based on previous results.⁷⁰ For squalane,
353 the bulk values and the surface O:C values are in good agreement, providing strong evidence that
354 the particle is well-mixed. However, the surface O:C ratio for octacosane increases much more
355 rapidly than that of squalane for similar changes in bulk composition. The surface of octacosane
356 reaches its maximum O:C ratio after ~ 0.4 bulk oxidation lifetime (i.e. 35% of octacosane in the
357 particle reacts). Assuming only octacosane at the surface reacts and there is no internal diffusion,
358 this leads to a ca. 12 nm oxidative crust on the particle (based on estimates of oxidized organic
359 carbon density).⁷⁹

360 The maximum possible O:C ratios at the particle surfaces were calculated from Eq. 2 to be
361 0.21 ± 0.04 and 0.19 ± 0.01 for squalane and octacosane, respectively. The bulk O:C ratios for

362 squalane and triacontane ($C_{30}H_{62}$, a linear hydrocarbon that is assumed to behave identically to
363 octacosane) have been measured previously at very high OH exposures. In this previous
364 measurement, the bulk O:C ratio for squalane was measured to increase to ~ 0.3 after 16 bulk
365 oxidation lifetimes.⁷⁰ This is significantly larger than the maximum O:C ratio predicted here,
366 presumably due to the limited number of bulk oxidation lifetimes (i.e. a plateau O:C ratio was not
367 achieved for squalane).

368 In contrast with squalane, the surface composition of octacosane reached a steady value
369 with the OH exposures used here. Previous modeling results have predicted that as I_{RD} increases,
370 the particle starts eroding as fragmentation dominates the overall chemistry, and ketones and
371 carboxylic acids accumulate at the surface.²⁶ In addition, previous measurements have found the
372 bulk O:C ratio for triacontane to increase to >0.9 with an OH exposure of 1×10^{13} molecule $s^{-1} cm^{-2}$
373 ^{3,64} This is significantly different than what is observed here (maximum surface O:C ratio of
374 0.19 ± 0.01). Additionally, no products were observed in the bulk AMS measurements reported here
375 that would be consistent with such a large bulk O:C ratio (Figure 2d). The bulk elemental
376 composition in previous studies was determined indirectly using a high resolution AMS with an
377 electron impact ionization source.⁸² A recent report has summarized the change in average carbon
378 oxidation state with increasing OH exposure for many different particles (from solid to liquid,
379 saturated to unsaturated, etc.).⁶³ Despite its small effective uptake coefficient and low bulk
380 reactivity, triacontane particles were reported to have the largest and fastest change in bulk
381 chemical composition when compared to any other type of particle measured. It is possible particle
382 morphology, environmental conditions (such as RH), size and plasticization (discussed below)
383 could all impact how particle composition evolves with increased heterogeneous oxidation.

384 However, it is unclear how to understand the differences between the particle compositions
385 measured here and in previous results.

386 A reaction-diffusion model for the heterogeneous oxidation of triacontane by OH was
387 created to try to understand the previous bulk measurements.⁶⁴ The only way to obtain the large
388 bulk O:C ratios was to assume that the particles plasticized and diffusion timescales in the particle
389 decreased with increasing oxidation (i.e. I_{RD} decreased). Plasticization was built into the model by
390 assuming reaction products had a larger diffusion coefficient than that of triacontane. With
391 plasticization of the particle, the internal mixing timescales were faster than would be expected
392 from the self-diffusion coefficient of pure triacontane. As a result, reaction products diffused faster
393 and the particle was more homogeneously oxidized. When diffusion in the particle was kept
394 constant at the self-diffusion coefficient of triacontane, only the top ~1 nm at the surface was
395 oxidized and a highly oxidized crust was formed. Because products from oxidation were confined
396 to the surface, the maximum bulk O:C ratio under these conditions was ~0.1 (which did not support
397 the previous bulk measurements).⁶⁴

398 To understand the results presented here, two additional triacontane simulations were run
399 using the particle diameter and at the OH exposures measured here. As previously described,
400 heterogeneous oxidation is simulated using a multi-compartment model with built-in diffusion
401 pathways. Heterogeneous chemistry, bulk chemistry, diffusion and evaporation rates are all
402 explicitly stated using literature values when possible.⁶⁴ The model was run using Kinetiscope,
403 which is a stochastic kinetics simulator.⁸³ At each OH exposure, the spatially resolved distribution
404 of the O:C ratios was recorded. The internal distributions of the O:C ratio at an OH exposure of
405 5.0×10^{12} molecule s cm^{-3} using the plasticization model and the constant diffusion model are
406 shown in Figure 8a and 8b, respectively. As discussed, oxygenated molecules are allowed to

407 diffuse faster in the plasticization model. As a result, the contrast between surface and bulk
408 composition is not as extreme as it is in the constant diffusion model.

409 The EALs in organic nanoparticles for electrons with >2 eV KE were previously measured
410 to be ~3-4 nm.⁵² Thus, a depth-averaged O:C ratio can be calculated from each of the simulations
411 using estimates of the EAL (i.e. the experimental probing depth). From the simulated distribution
412 of O:C ratios [$OC(r)$], the depth-averaged O:C ratio (OC_m) obtained by XAS is predicted to be

$$413 \quad OC_m = \int_0^R OC(r)e^{-r/EAL} dr / \int_0^R e^{-r/EAL} dr, \quad (4)$$

414 where R is the radius of the particle and r is the distance from the surface of the particle. At longer
415 EALs, the XAS probe is less surface sensitive and more material from the core of the particle is
416 probed. The depth-averaged O:C ratios calculated using different estimated EALs (2, 4, 6, 8 and
417 10 nm) are shown in Figure 8c and 8d for the plasticization and constant diffusion models,
418 respectively.

419 With plasticization, oxidized reaction products can diffuse faster, which results in a less
420 steep chemical gradient within the particle (as shown in Figure 8a). Because new reaction products
421 are still probed at longer EALs, changing the EAL has less of an effect on changing the depth-
422 averaged O:C ratio. For example, at an OH exposure of 5×10^{12} molecule s cm^{-3} , the depth averaged
423 O:C ratio only decreases from 0.65 to 0.40 when the EAL increases from 2 to 10 nm. The
424 experimental O:C ratios measured with the XAS probe are overlaid on the depth-averaged O:C
425 ratios from the plasticization model in Figure 8c. As expected, the plasticization model (which
426 more closely fits the previous bulk measurements) over-predicts O:C ratio at all estimated EALs.
427 Additionally, the depth-averaged O:C ratios continuously increase over the range of OH exposures
428 simulated. This does not match the functional form of the experimental data observed here, which
429 reaches a plateau at OH exposures larger than 1×10^{12} molecule s cm^{-3} .

430 Without plasticization, diffusion is uniformly slow and reaction products are confined to
431 the interface (as shown in Figure 8b). Even though the model predicts O:C ratios that are >1 at the
432 surface of the particle, the measured O:C ratio decreases significantly when contributions from the
433 subsurface of the particle are included because the oxidized layer is only ~ 1 nm thick. For example,
434 at an OH exposure of 5×10^{12} molecule s cm^{-3} , the depth averaged O:C ratio decreases from 0.56 to
435 0.12 when the EAL increases from 2 to 10 nm. The experimental O:C ratios are overlaid on the
436 depth-averaged O:C ratios from the constant diffusion model in Figure 8d. This model accurately
437 predicts the measured O:C ratio assuming an EAL of ~ 8 nm, which is reasonable given the strong
438 material dependence on electron scattering at low KEs.⁵² In addition, the depth-averaged O:C
439 ratios plateau over the range of OH exposures simulated because all of the oxygenated species in
440 the particle are probed at each EAL. This matches the functional form of the experimental data.
441 Thus, the experimental results measured here suggest that aerosol particles composed of long
442 linear hydrocarbons form a highly oxidized crust when they are heterogeneously oxidized,
443 suggesting that an extremely steep chemical gradient is formed within the particle.

444 **IV. Conclusions:**

445 Photoemission spectroscopy was used to study the changing surface composition and the
446 formation of chemical gradients during a heterogeneous reaction. The heterogeneous oxidation of
447 both highly viscous octacosane and liquid squalane particles were compared using both bulk and
448 surface measurements. In bulk measurements, pure octacosane particles were found to react much
449 more slowly than pure squalane particles. In mixtures of octacosane and squalane, reaction kinetics
450 were dependent on initial particle composition. When the composition of squalane was high ($x_{\text{sqa}} > 0.8$),
451 diffusion was fast relative to the reaction frequency, and octacosane and squalane reacted
452 with the same fast rates (i.e. $I_{RD} \ll 1$). As the squalane composition decreased ($0.6 < x_{\text{sqa}} < 0.8$),

453 diffusion started to slow relative to reaction frequency, and octacosane and squalane reacted with
454 the same slower rates (i.e. $I_{RD} \sim 1$). At low squalane composition ($x_{\text{sqa}} < 0.6$), squalane and
455 octacosane reaction rates diverged and approached the values measured for their pure states, due
456 to phase separation.

457 The formation of chemical gradients in the particles were measured using XAS at the
458 carbon and oxygen K edges. In these surface sensitive probes, octacosane appeared to
459 heterogeneously react significantly faster than squalane particles, demonstrating that even though
460 the bulk composition of octacosane changed slowly, the surface composition changed much more
461 rapidly. Using the oxygen K edge XAS spectra, the change in the O:C ratio of the surface region
462 could be probed directly. From the kinetics of the O:C ratio, the data reported here suggest that
463 diffusion in the octacosane particle remains very slow and only the molecules at the surface of the
464 particle react, creating a highly oxidized crust around an unoxidized core. This conclusion is
465 supported by the bulk AMS measurements reported here, wherein products of heterogeneous
466 oxidation were below the detection limit. The conclusion is also supported by previous work
467 looking at the products of heterogeneous oxidation of octacosane. This work found that only the
468 ends of the octacosane molecule reacted, suggesting that the molecules were frozen at the particle's
469 surface.¹⁹ The measurements reported here suggest that the bulk O:C ratio of octacosane particles
470 does not increase as rapidly as that of liquid squalane particles.

471 Previous work looking at heterogeneous oxidation has observed much larger changes in
472 bulk composition of particles composed of linear alkanes.^{63,64} The kinetic model created in this
473 previous work could explain the data measured here by assuming particles do not plasticize with
474 increased oxidation.⁶⁴ The differences between the previous measurements and those reported here

475 cannot be readily rationalized, but particle morphology or some other environmental factor (such
476 as relative humidity) could play a role in either promoting or inhibiting plasticization.

477 Ultimately, this work demonstrates that diffusion limitations can create particles with
478 highly oxidized surfaces at relatively low oxidant exposures. By changing the chemical nature of
479 the interface, it is expected the atmospheric fate of these diffusion-limited particles will change.

480 **Supporting Information:**

481 Details of measuring effective uptake coefficients in mixtures; OH radical reaction
482 mechanism; Reference carbon K edge XAS spectra; O:C ratio calibration curve from oxygen K
483 edge XAS spectra.

484 **Acknowledgments:**

485 This work is supported by the Chemical Sciences Geosciences and Biosciences Division
486 of the Office of Basic Energy Sciences of the U.S. Department of Energy under Contract No. DE-
487 AC02-05CH11231. M.I.J. was supported by a NSF Graduate Research Fellowship under DGE-
488 1106400. F.A.H and A.A.W. were supported by the Laboratory Directed Research and
489 Development program at Lawrence Berkeley National Laboratory under U. S. Department of
490 Energy Office of Science, Office of Basic Energy Sciences under Contract No. DE-AC02-
491 05CH11231. This research used resources of the Advanced Light Source, which is a DOE Office
492 of Science User Facility under contract no. DE-AC02-05CH11231.

493 **References:**

494

495 (1) Virtanen, A.; Joutsensaari, J.; Koop, T.; Kannosto, J.; Yli-Pirilä, P.; Leskinen, J.; Mäkelä,
496 J. M.; Holopainen, J. K.; Pöschl, U.; Kulmala, M.; et al. An Amorphous Solid State of
497 Biogenic Secondary Organic Aerosol Particles. *Nature* **2010**, *467* (7317), 824–827 DOI:
498 10.1038/nature09455.

499 (2) Roth, C. M.; Goss, K. U.; Schwarzenbach, R. P. Sorption of a Diverse Set of Organic
500 Vapors to Diesel Soot and Road Tunnel Aerosols. *Environ. Sci. Technol.* **2005**, *39* (17),
501 6632–6637 DOI: 10.1021/es049204w.

502 (3) Koop, T.; Bookhold, J.; Shiraiwa, M.; Pöschl, U. Glass Transition and Phase State of
503 Organic Compounds: Dependency on Molecular Properties and Implications for
504 Secondary Organic Aerosols in the Atmosphere. *Phys. Chem. Chem. Phys.* **2011**, *13* (43),
505 19238–19255 DOI: 10.1039/c1cp22617g.

506 (4) Reid, J. P.; Bertram, A. K.; Topping, D. O.; Laskin, A.; Martin, S. T.; Petters, M. D.;
507 Pope, F. D.; Rovelli, G. The Viscosity of Atmospherically Relevant Organic Particles.
508 *Nat. Commun.* **2018**, *9*, 1–14 DOI: 10.1038/s41467-018-03027-z.

509 (5) Jimenez, J. L.; Canagaratna, M. R.; Donahue, N. M.; Prevot, A. S. H.; Zhang, Q.; Kroll, J.
510 H.; DeCarlo, P. F.; Allan, J. D.; Coe, H.; Ng, N. L.; et al. Evolution of Organic Aerosols
511 in the Atmosphere. *Science (80-.)*. **2009**, *326* (5959), 1525–1529 DOI:
512 10.1126/science.1180353.

513 (6) Farmer, D. K.; Cappa, C. D.; Kreidenweis, S. M. Atmospheric Processes and Their
514 Controlling Influence on Cloud Condensation Nuclei Activity. *Chem. Rev.* **2015**, *115*,
515 4199–4217 DOI: 10.1021/cr5006292.

516 (7) Ruehl, C. R.; Davies, J. F.; Wilson, K. R. An Interfacial Mechanism for Cloud Droplet
517 Formation on Organic Aerosols. *Science (80-.)*. **2016**, *351* (6280), 1447.

518 (8) Pajunoja, A.; Lambe, A. T.; Hakala, J.; Rastak, N.; Cummings, M. J.; Brogan, J. F.; Hao,
519 L.; Paramonov, M.; Hong, J.; Prisle, N. L.; et al. Adsorptive Uptake of Water by
520 Semisolid Secondary Organic Aerosols In the atmosphere. *Nat. Geosci.* **2014**, *42*, 1–6
521 DOI: 10.1002/2015GL063142.Received.

522 (9) Gray Bé, A.; Upshur, M. A.; Liu, P.; Martin, S. T.; Geiger, F. M.; Thomson, R. J. Cloud
523 Activation Potentials for Atmospheric α -Pinene and β -Caryophyllene Ozonolysis
524 Products. *ACS Cent. Sci.* **2017**, *3* (7), 715–725 DOI: 10.1021/acscentsci.7b00112.

525 (10) Chan, M. N.; Zhang, H.; Goldstein, A. H.; Wilson, K. R. Role of Water and Phase in the
526 Heterogeneous Oxidation of Solid and Aqueous Succinic Acid Aerosol by Hydroxyl
527 Radicals. *J. Phys. Chem. C* **2014**, *118*, 28978–28992 DOI: 10.1021/jp5012022.

528 (11) Jonathan H. Slade and Daniel A. Knopf. Multiphase OH Oxidation Kinetics of Organic
529 Aerosol: The Role of Particle Phase State and Relative Humidity. *Geophys. Res. Lett.*
530 **2015**, *41*, 5297–5306 DOI: 10.1002/2014GL060582.Received.

531 (12) Arangio, A. M.; Slade, J. H.; Berkemeier, T.; Pöschl, U.; Knopf, D. A.; Shiraiwa, M.
532 Multiphase Chemical Kinetics of OH Radical Uptake by Molecular Organic Markers of
533 Biomass Burning Aerosols: Humidity and Temperature Dependence, Surface Reaction,
534 and Bulk Diffusion. *J. Phys. Chem. A* **2015**, *119* (19), 4533–4544 DOI:
535 10.1021/jp510489z.

536 (13) Moise, T.; Rudich, Y. Reactive Uptake of Ozone by Aerosol-associated Unsaturated Fatty
537 Acids: Kinetics, Mechanism, and Products. *J. Phys. Chem. A* **2002**, *106* (27), 6469–6476
538 DOI: 10.1021/jp025597e.

- 539 (14) Davies, J. F.; Wilson, K. R. Nanoscale Interfacial Gradients Formed by the Reactive
540 Uptake of OH Radicals onto Viscous Aerosol Surfaces. *Chem. Sci.* **2015**, *6* (12), 7020–
541 7027 DOI: 10.1039/C5SC02326B.
- 542 (15) Shiraiwa, M.; Ammann, M.; Koop, T.; Pöschl, U. Gas Uptake and Chemical Aging of
543 Semisolid Organic Aerosol Particles. *Proc. Natl. Acad. Sci. U. S. A.* **2011**, *108* (27),
544 11003–11008 DOI: 10.1073/pnas.1103045108.
- 545 (16) Berkemeier, T.; Steimer, S. S.; Krieger, U. K.; Peter, T.; Pöschl, U.; Ammann, M.;
546 Shiraiwa, M. Ozone Uptake on Glassy, Semi-Solid and Liquid Organic Matter and the
547 Role of Reactive Oxygen Intermediates in Atmospheric Aerosol Chemistry. *Phys. Chem.*
548 *Chem. Phys.* **2016**, *18* (18), 12662–12674 DOI: 10.1039/C6CP00634E.
- 549 (17) Steimer, S. S.; Berkemeier, T.; Gilgen, A.; Krieger, U. K.; Peter, T.; Shiraiwa, M.;
550 Ammann, M. Shikimic Acid Ozonolysis Kinetics of the Transition from Liquid Aqueous
551 Solution to Highly Viscous Glass. *Phys. Chem. Chem. Phys.* **2015**, *17* (46), 31101–31109
552 DOI: 10.1039/C5CP04544D.
- 553 (18) Marshall, F. H.; Berkemeier, T.; Shiraiwa, M.; Nandy, L.; Ohm, P. B.; Dutcher, C. S.;
554 Reid, J. P. Influence of Particle Viscosity on Mass Transfer and Heterogeneous
555 Ozonolysis Kinetics in Aqueous-Sucrose-Maleic Acid Aerosol. *Phys. Chem. Chem. Phys.*
556 **2018**, *20* (22), 15560–15573 DOI: 10.1039/c8cp01666f.
- 557 (19) Ruehl, C.; Nah, T.; Isaacman, G.; Worton, D.; Chan, A. W. H.; Kolesar, K. R.; Cappa, C.
558 D.; Goldstein, A. H.; Wilson, K. R. The Influence of Molecular Structure and Aerosol
559 Phase on the Heterogeneous Oxidation of Normal and Branched Alkanes by OH. *J. Phys.*
560 *Chem. A* **2013**, *117*, 3990–4000.
- 561 (20) Kuwata, M.; Martin, S. T. Phase of Atmospheric Secondary Organic Material Affects its
562 Reactivity. *Proc. Natl. Acad. Sci. U. S. A.* **2012**, *109* (43), 17354–17359 DOI:
563 10.1073/pnas.1209071109.
- 564 (21) Zhou, S.; Shiraiwa, M.; McWhinney, R. D.; Pöschl, U.; Abbatt, J. P. D. Kinetic
565 Limitations in Gas-Particle Reactions Arising from Slow Diffusion in Secondary Organic
566 Aerosol. *Faraday Discuss.* **2013**, *165*, 391–406 DOI: 10.1039/c3fd00030c.
- 567 (22) Allan, M.; Bagot, P. A. J.; Westacott, R. E.; Costen, M. L.; Mckendrick, K. G. Influence
568 of Molecular and Supramolecular Structure on the Gas-Liquid Interfacial Reactivity of
569 Hydrocarbon Liquids with O (3P) Atoms. *J. Phys. Chem. C* **2008**, *112*, 1524–1532 DOI:
570 10.1021/jp076441n.
- 571 (23) Lee, L.; Wilson, K. The Reactive–Diffusive Length of OH and Ozone in Model Organic
572 Aerosols. *J. Phys. Chem. A* **2016**, *120* (34), 6800–6812 DOI: 10.1021/acs.jpca.6b05285.
- 573 (24) Houle, F. A.; Hinsberg, W. D.; Wilson, K. R. Oxidation of a Model Alkane Aerosol by
574 OH Radical: The Emergent Nature of Reactive Uptake. *Phys. Chem. Chem. Phys.* **2015**,
575 *17* (6), 4412–4423 DOI: 10.1039/c4cp05093b.
- 576 (25) Houle, F. A.; Wiegel, A. A.; Wilson, K. R. Changes in Reactivity as Chemistry Becomes
577 Confined to an Interface. The Case of Free Radical Oxidation of C₃₀H₆₂ Alkane by
578 OH. *J. Phys. Chem. Lett.* **2018**, *9*, 1053–1057 DOI: 10.1021/acs.jpcllett.8b00172.
- 579 (26) Houle, F. A.; Wiegel, A. A.; Wilson, K. R. Predicting Aerosol Reactivity Across Scales:
580 from the Laboratory to the Atmosphere. *Environ. Sci. Technol.* **2018**, *52*, 13774–13781
581 DOI: 10.1021/acs.est.8b04688.
- 582 (27) Pfrang, C.; Shiraiwa, M.; Pöschl, U. Chemical Ageing and Transformation of Diffusivity
583 in Semi-Solid Multi-Component Organic Aerosol Particles. *Atmos. Chem. Phys.* **2011**, *11*
584 (14), 7343–7354 DOI: 10.5194/acp-11-7343-2011.

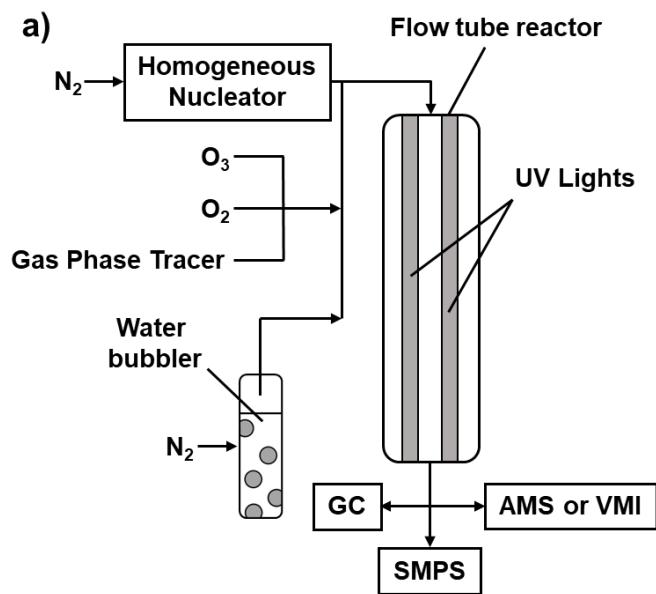
- 585 (28) Jayne, J. T.; Leard, D. C.; Zhang, X.; Davidovits, P.; Smith, K. a.; Kolb, C. E.; Worsnop,
586 D. R. Development of an Aerosol Mass Spectrometer for Size and Composition Analysis
587 of Submicron Particles. *Aerosol Sci. Technol.* **2000**, *33* (1–2), 49–70 DOI:
588 10.1080/027868200410840.
- 589 (29) Maria, S. F.; Russell, L. M.; Gilles, M. K.; Myneni, S. C. B. Organic Aerosol Growth
590 Mechanisms and Their Climate-Forcing Implications. *Science (80-.)*. **2004**, *306* (5703),
591 1921–1924 DOI: 10.1126/science.1103491.
- 592 (30) Laskin, A.; Iedema, M. J.; Cowin, J. P. Time-Resolved Aerosol Collector for
593 CCSEM/EDX Single-Particle Analysis. *Aerosol Sci. Technol.* **2003**, *37* (3), 246–260 DOI:
594 10.1080/02786820300945.
- 595 (31) Pratt, K. A.; Prather, K. A. Mass Spectrometry of Atmospheric Aerosols-Recent
596 Developments and Applications. Part I: Off-line Mass Spectrometry Techniques. *Mass*
597 *Spectrom. Rev.* **2012**, *31*, 1–16 DOI: 10.1002/mas.20322.
- 598 (32) Lim, C. Y.; Browne, E. C.; Sugrue, R. A.; Kroll, J. H. Rapid Heterogeneous Oxidation of
599 Organic Coatings on Submicron Aerosols. *Geophys. Res. Lett.* **2017**, *44* (6), 2949–2957
600 DOI: 10.1002/2017GL072585.
- 601 (33) Chan, M. N.; Nah, T.; Wilson, K. R. Real Time in Situ Chemical Characterization of Sub-
602 Micron Organic Aerosols Using Direct Analysis in Real Time Mass Spectrometry
603 (DART-MS): The Effect of Aerosol Size and Volatility. *Analyst* **2013**, *138* (13), 3749
604 DOI: 10.1039/c3an00168g.
- 605 (34) Nah, T.; Chan, M.; Leone, S. R.; Wilson, K. R. Real Time in Situ Chemical
606 Characterization of Submicrometer Organic Particles using Direct Analysis in Real Time-
607 Mass Spectrometry. *Anal. Chem.* **2013**, *85* (4), 2087–2095 DOI: 10.1021/ac302560c.
- 608 (35) Zhao, Y.; Fairhurst, M. C.; Wingen, L. M.; Perraud, V.; Ezell, M. J.; Finlayson-Pitts, B. J.
609 New Insights Into Atmospherically Relevant Reaction Systems Using Direct Analysis in
610 Real-Time Mass Spectrometry (DART-MS). *Atmos. Meas. Tech.* **2017**, *10* (4), 1373–1386
611 DOI: 10.5194/amt-10-1373-2017.
- 612 (36) Kumbhani, S.; Longin, T.; Wingen, L. M.; Kidd, C.; Perraud, V.; Finlayson-Pitts, B. J.
613 New Mechanism of Extractive Electrospray Ionization Mass Spectrometry for
614 Heterogeneous Solid Particles. *Anal. Chem.* **2018**, *90*, 2055–2062 DOI:
615 10.1021/acs.analchem.7b04164.
- 616 (37) Wingen, L. M.; Finlayson-Pitts, B. J. Probing Surfaces of Atmospherically Relevant
617 Organic Particles by Easy Ambient Sonic-Spray Ionization Mass Spectrometry (EASI-
618 MS). *Chem. Sci.* **2019**, *10*, 884–897 DOI: 10.1039/c8sc03851a.
- 619 (38) Wu, Y.; Li, W.; Xu, B.; Li, X.; Wang, H.; McNeill, V. F.; Rao, Y.; Dai, H. L. Observation
620 of Organic Molecules at the Aerosol Surface. *J. Phys. Chem. Lett.* **2016**, *7* (12), 2294–
621 2297 DOI: 10.1021/acs.jpcclett.6b00872.
- 622 (39) Ebben, C. J.; Ault, A. P.; Ruppel, M. J.; Ryder, O. S.; Bertram, T. H.; Grassian, V. H.;
623 Prather, K. A.; Geiger, F. M. Size-Resolved Sea Spray Aerosol Particles Studied by
624 Vibrational Sum Frequency Generation. *J. Phys. Chem. A* **2013**, *117*, 6589–6601 DOI:
625 10.1021/jp401957k.
- 626 (40) Martinez, I. S.; Peterson, M. D.; Ebben, C. J.; Hayes, P. L.; Artaxo, P.; Martin, S. T.;
627 Geiger, F. M.; Hemminger, J.; Tobias, D. On Molecular Chirality Within Naturally
628 Occurring Secondary Organic Aerosol Particles from the Central Amazon Basin. *Phys.*
629 *Chem. Chem. Phys.* **2011**, *13*, 12114–12122 DOI: 10.1039/c1cp20428a.
- 630 (41) Wilson, K. R.; Bluhm, H.; Ahmed, M. Aerosol Photoemission. In *Fundamentals and*

- 631 *Applications in Aerosol Spectroscopy*; Signorell, R., Reid, J. P., Eds.; CRC Press: Boca
632 Raton, FL, 2011; pp 367–400.
- 633 (42) Wilson, K. R.; Peterka, D. S.; Jimenez-Cruz, M.; Leone, S. R.; Ahmed, M. VUV
634 Photoelectron Imaging of Biological Nanoparticles: Ionization Energy Determination of
635 Nanophase Glycine and Phenylalanine-Glycine-Glycine. *Phys. Chem. Chem. Phys.* **2006**,
636 8 (16), 1884–1890 DOI: 10.1039/b517487b.
- 637 (43) Wilson, K. R.; Zou, S.; Shu, J.; Rühl, E.; Leone, S. R.; Schatz, G. C.; Ahmed, M. Size-
638 Dependent Angular Distributions of Low-Energy Photoelectrons Emitted from NaCl
639 Nanoparticles. *Nano Lett.* **2007**, 7 (7), 2014–2019 DOI: 10.1021/nl070834g.
- 640 (44) Lin, P.-C.; Wu, Z.-H.; Chen, M.-S.; Li, Y.-L.; Chen, W.-R.; Huang, T.-P.; Lee, Y.; Wang,
641 C. C. Interfacial Solvation and Surface pH of Phenol and Dihydroxybenzene Aqueous
642 Nanoaerosols Unveiled by Aerosol VUV Photoelectron Spectroscopy. *J. Phys. Chem. B*
643 **2017**, 121 (5), 1054–1067 DOI: 10.1021/acs.jpcc.6b10201.
- 644 (45) Woods, E.; Konys, C. A.; Rossi, S. R. Photoemission of Iodide from Aqueous Aerosol
645 Particle Surfaces. *J. Phys. Chem. A* **2019**, 123, 2901–2907 DOI:
646 10.1021/acs.jpca.8b12323.
- 647 (46) Berg, M. J.; Wilson, K. R.; Sorensen, C. M.; Chakrabarti, A.; Ahmed, M. Discrete Dipole
648 Approximation for Low-Energy Photoelectron Emission from NaCl Nanoparticles. *J.*
649 *Quant. Spectrosc. Radiat. Transf.* **2012**, 113 (3), 259–265 DOI:
650 10.1016/j.jqsrt.2011.10.007.
- 651 (47) Goldmann, M.; Miguel-Sánchez, J.; West, A. H. C.; Yoder, B. L.; Signorell, R. Electron
652 Mean Free Path from Angle-Dependent Photoelectron Spectroscopy of Aerosol Particles.
653 *J. Chem. Phys.* **2015**, 142, 224304 DOI: 10.1063/1.4922307.
- 654 (48) West, A. H. C.; Yoder, B. L.; Signorell, R. Size-Dependent Velocity Map Photoelectron
655 Imaging of Nanosized Ammonia Aerosol Particles. *J. Phys. Chem. A* **2013**, 117 (50),
656 13326–13335 DOI: 10.1021/jp406313a.
- 657 (49) Shu, J.; Wilson, K. R.; Ahmed, M.; Leone, S. R. Coupling a Versatile Aerosol Apparatus
658 to a Synchrotron: Vacuum Ultraviolet Light Scattering, Photoelectron Imaging, and
659 Fragment Free Mass Spectrometry. *Rev. Sci. Instrum.* **2006**, 77 (4), 0–10 DOI:
660 10.1063/1.2194474.
- 661 (50) Signorell, R.; Goldmann, M.; Yoder, B. L.; Bodi, A.; Chasovskikh, E.; Lang, L.;
662 Luckhaus, D. Nanofocusing, Shadowing, and Electron Mean Free Path in the
663 Photoemission from Aerosol Droplets. *Chem. Phys. Lett.* **2016**, 658, 1–6 DOI:
664 10.1016/j.cplett.2016.05.046.
- 665 (51) Jacobs, M. I.; Xu, B.; Kostko, O.; Heine, N.; Ahmed, M.; Wilson, K. R. Probing the
666 Heterogeneous Ozonolysis of Squalene Nanoparticles by Photoemission. *J. Phys. Chem. A*
667 **2016**, 120 (43), 8645–8656 DOI: 10.1021/acs.jpca.6b09061.
- 668 (52) Jacobs, M. I.; Kostko, O.; Ahmed, M.; Wilson, K. R. Low Energy Electron Attenuation
669 Lengths in Core-Shell Nanoparticles. *Phys. Chem. Chem. Phys.* **2017**, 19 (20), 13372–
670 13378 DOI: 10.1039/C7CP00663B.
- 671 (53) Xiong, W.; Hickstein, D. D.; Schnitzenbaumer, K. J.; Ellis, J. L.; Palm, B. B.; Keister, K.
672 E.; Ding, C.; Miaja-Avila, L.; Dukovic, G.; Jimenez, J. L.; et al. Photoelectron
673 Spectroscopy of CdSe Nanocrystals in the Gas Phase: A Direct Measure of the Evanescent
674 Electron Wave Function of Quantum Dots. *Nano Lett.* **2013**, 13 (6), 2924–2930 DOI:
675 10.1021/nl401309z.
- 676 (54) Mysak, E. R.; Starr, D. E.; Wilson, K. R.; Bluhm, H. Note: A Combined Aerodynamic

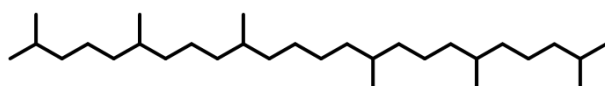
- 677 Lens/Ambient Pressure X-ray Photoelectron Spectroscopy Experiment for the On-Stream
678 Investigation of Aerosol Surfaces. *Rev. Sci. Instrum.* **2010**, *81* (1), 016106 DOI:
679 10.1063/1.3276714.
- 680 (55) Antonsson, E.; Patanen, M.; Nicolas, C.; Neville, J. J.; Benkoula, S.; Goel, A.; Miron, C.
681 Complete Bromide Surface Segregation in Mixed NaCl/NaBr Aerosols Grown from
682 Droplets. *Phys. Rev. X* **2015**, *5*, 011025 DOI: 10.1103/PhysRevX.5.011025.
- 683 (56) Benkoula, S.; Sublemontier, O.; Patanen, M.; Nicolas, C.; Sirotti, F.; Naitabdi, A.; Gaie-
684 Levrel, F.; Antonsson, E.; Aureau, D.; Ouf, F.-X.; et al. Water Adsorption on TiO₂
685 Surfaces Probed by Soft X-ray Spectroscopies: Bulk materials vs. Isolated Nanoparticles.
686 *Sci. Rep.* **2015**, *5* (1), 1–11 DOI: 10.1038/srep15088.
- 687 (57) Antonsson, E.; Langer, B.; Halfpap, I.; Gottwald, J.; Rühl, E. Photoelectron Angular
688 Distribution from Free SiO₂ Nanoparticles as a Probe of Elastic Electron Scattering. *J.*
689 *Chem. Phys.* **2017**, *146* (24), 244301 DOI: 10.1063/1.4986406.
- 690 (58) Meinen, J.; Khasminskaya, S.; Eritt, M.; Leisner, T.; Antonsson, E.; Langer, B.; Rühl, E.
691 Core Level Photoionization on Free Sub-10-nm Nanoparticles Using Synchrotron
692 Radiation. *Rev. Sci. Instrum.* **2010**, *81* (8), 085107 DOI: 10.1063/1.3475154.
- 693 (59) Sublemontier, O.; Nicolas, C.; Aureau, D.; Patanen, M.; Kintz, H.; Liu, X.; Gaveau, M.;
694 Garrec, J. Le; Robert, E.; Barreda, F. X-ray Photoelectron Spectroscopy of Isolated
695 Nanoparticles. *J. Phys. Chem. Lett.* **2014**, *5*, 3399–3403 DOI: 10.1021/jz501532c.
- 696 (60) Kostko, O.; Xu, B.; Jacobs, M. I.; Ahmed, M. Soft X-ray Spectroscopy of Nanoparticles
697 by Velocity Map Imaging. *J. Chem. Phys.* **2017**, *147* (1), 013931 DOI:
698 10.1063/1.4982822.
- 699 (61) Xu, B.; Jacobs, M. I.; Kostko, O.; Ahmed, M. Guanidinium Group is Protonated in a
700 Strongly Basic Arginine Solution. *ChemPhysChem* **2017**, *18*, 1503–1506 DOI:
701 10.1002/cphc.201700197.
- 702 (62) Ouf, F.-X.; Parent, P.; Laffon, C.; Marhaba, I.; Ferry, D.; Marcillaud, B.; Antonsson, E.;
703 Benkoula, S.; Liu, X.-J.; Nicolas, C.; et al. First In-Flight Synchrotron X-ray Absorption
704 and Photoemission Study of Carbon Soot Nanoparticles. *Sci. Rep.* **2016**, *6* (October),
705 36495 DOI: 10.1038/srep36495.
- 706 (63) Kroll, J. H.; Lim, C. Y.; Kessler, S. H.; Wilson, K. R. Heterogeneous Oxidation of
707 Atmospheric Organic Aerosol: Kinetics of Changes to the Amount and Oxidation State of
708 Particle-Phase Organic Carbon. *J. Phys. Chem. A* **2015**, *119* (55), 10767–10783 DOI:
709 10.1021/acs.jpca.5b06946.
- 710 (64) Wiegel, A. A.; Liu, M. J.; Hinsberg, W. D.; Wilson, K. R.; Houle, F. A. Diffusive
711 Confinement of Free Radical Intermediates in the OH Radical Oxidation of Semisolid
712 Aerosols. *Phys. Chem. Chem. Phys.* **2017**, *19* (9), 6814–6830 DOI: 10.1039/c7cp00696a.
- 713 (65) Smith, J. D.; Kroll, J. H.; Cappa, C. D.; Che, D. L.; Liu, C. L.; Ahmed, M.; Leone, S. R.;
714 Worsnop, D. R.; Wilson, K. R. The Heterogeneous Reaction of Hydroxyl Radicals with
715 Sub-Micron Squalane Particles: A Model System for Understanding the Oxidative Aging
716 of Ambient Aerosols. *Atmos. Chem. Phys.* **2009**, *9* (9), 3209–3222 DOI: 10.5194/acp-9-
717 3209-2009.
- 718 (66) Atkinson, R.; Baulch, D. L.; Cox, R. a.; Crowley, J. N.; Hampson, R. F.; Hynes, R. G.;
719 Jenkin, M. E.; Rossi, M. J.; Troe, J. Evaluated Kinetic and Photochemical Data for
720 Atmospheric Chemistry: Volume III – Gas Phase Reactions of Inorganic Halogens.
721 *Atmos. Chem. Phys.* **2007**, *7*, 981–1191 DOI: 10.5194/acp-7-981-2007.
- 722 (67) Gloaguen, E.; Mysak, E. R.; Leone, S. R.; Ahmed, M.; Wilson, K. R. Investigating the

- 723 Chemical Composition of Mixed Organic-Inorganic Particles by “Soft” Vacuum
724 Ultraviolet Photoionization: The Reaction of Ozone with Anthracene on Sodium Chloride
725 Particles. *Int. J. Mass Spectrom.* **2006**, *258* (1–3), 74–85 DOI:
726 10.1016/j.ijms.2006.07.019.
- 727 (68) Dribinski, V.; Ossadtchi, A.; Mandelshtam, V. a.; Reisler, H. Reconstruction of Abel-
728 Transformable Images: The Gaussian Basis-Set Expansion Abel Transform Method. *Rev.*
729 *Sci. Instrum.* **2002**, *73* (7), 2634 DOI: 10.1063/1.1482156.
- 730 (69) Wiegel, A. a.; Wilson, K. R.; Hinsberg, W. D.; Houle, F. a. Stochastic Methods for
731 Aerosol Chemistry: A Compact Molecular Description of Functionalization and
732 Fragmentation in the Heterogeneous Oxidation of Squalane Aerosol by OH Radicals.
733 *Phys. Chem. Chem. Phys.* **2015**, *17*, 4398–4411 DOI: 10.1039/C4CP04927F.
- 734 (70) Kroll, J. H.; Smith, J. D.; Che, D. L.; Kessler, S. H.; Worsnop, D. R.; Wilson, K. R.
735 Measurement of Fragmentation and Functionalization Pathways in the Heterogeneous
736 Oxidation of Oxidized Organic Aerosol. *Phys. Chem. Chem. Phys.* **2009**, *11* (36), 7759
737 DOI: 10.1039/b916865f.
- 738 (71) Che, D. L.; Smith, J. D.; Leone, S. R.; Ahmed, M.; Wilson, K. R. Quantifying the
739 Reactive Uptake of OH by Organic Aerosols in a Continuous Flow Stirred Tank Reactor.
740 *Phys. Chem. Chem. Phys.* **2009**, *11*, 7885–7895 DOI: 10.1039/b916865f.
- 741 (72) Richards-Henderson, N. K.; Goldstein, A. H.; Wilson, K. R. Large Enhancement in the
742 Heterogeneous Oxidation Rate of Organic Aerosols by Hydroxyl Radicals in the Presence
743 of Nitric Oxide. *J. Phys. Chem. Lett.* **2015**, *6* (22), 4451–4455 DOI:
744 10.1021/acs.jpcclett.5b02121.
- 745 (73) Richards-Henderson, N. K.; Goldstein, A. H.; Wilson, K. R. Sulfur Dioxide Accelerates
746 the Heterogeneous Oxidation Rate of Organic Aerosol by Hydroxyl Radicals. *Environ.*
747 *Sci. Technol.* **2016**, *50* (7), 3554–3561 DOI: 10.1021/acs.est.5b05369.
- 748 (74) Katrib, Y.; Biskos, G.; Buseck, P. R.; Davidovits, P.; Jayne, J. T.; Mochida, M.; Wise, M.
749 E.; Worsnop, D. R.; Martin, S. T. Ozonolysis of Mixed Oleic-Acid/Stearic-Acid Particles :
750 Reaction Kinetics and Chemical Morphology. *J. Phys. Chem. A* **2005**, *109*, 10910–10919
751 DOI: 10.1021/jp054714d.
- 752 (75) Kwok, E. S. C.; Atkinson, R. Estimation of Hydroxyl Radical Reaction Rate Constants for
753 Gas-Phase Organic Compounds Using a Structure-Reactivity Relationship: An Update.
754 *Atmos. Environ.* **1995**, *29* (14), 1685–1695 DOI: 10.1016/1352-2310(95)00069-B.
- 755 (76) Heslot, F.; Cazabat, A. M.; Levinson, P. Dynamics of Wetting of Tiny Drops:
756 Ellipsometric Study of the Late Stages of Spreading. *Phys. Rev. Lett.* **1989**, *62* (11), 1286–
757 1289.
- 758 (77) Mysak, E. R.; Smith, J. D.; Ashby, P. D.; Newberg, J. T.; Wilson, K. R.; Bluhm, H.
759 Competitive Reaction Pathways for Functionalization and Volatilization in the
760 Heterogeneous Oxidation of Coronene Thin Films by Hydroxyl Radicals and Ozone.
761 *Phys. Chem. Chem. Phys.* **2011**, *13* (16), 7554–7564 DOI: 10.1039/c0cp02323j.
- 762 (78) Beamson, G.; Briggs, D. *High Resolution XPS of Organic Polymers: The Scienta*
763 *ESCA300 Database*; John Wiley & Sons, Inc.: Chichester, 1992.
- 764 (79) Wilson, K. R.; Smith, J. D.; Kessler, S. H.; Kroll, J. H. The Statistical Evolution of
765 Multiple Generations of Oxidation Products in the Photochemical Aging of Chemically
766 Reduced Organic Aerosol. *Phys. Chem. Chem. Phys.* **2012**, *14* (4), 1468–1479 DOI:
767 10.1039/c1cp22716e.
- 768 (80) Moffet, R. C.; Henn, T.; Laskin, A.; Gilles, M. K. Automated Chemical Analysis of

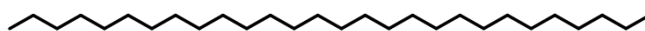
- 769 Internally Mixed Aerosol Particles Using X-ray Spectromicroscopy at the Carbon K-edge.
770 *Anal. Chem.* **2010**, *82* (19), 7906–7914 DOI: 10.1021/ac1012909.
- 771 (81) Hitchcock, A. P.; Mancini, D. C. Bibliography and Database of Inner Shell Excitation
772 Spectra of Gas Phase Atoms and Molecules. *J. Electron Spectros. Relat. Phenomena*
773 **1994**, *67*, 1–132.
- 774 (82) Aiken, A. C.; Decarlo, P. F.; Kroll, J. H.; Worsnop, D. R.; Huffman, J. A.; Docherty, K.
775 S.; Ulbrich, I. M.; Mohr, C.; Kimmel, J. R.; Sueper, D.; et al. O/C and OM/OC Ratios of
776 Primary, Secondary, and Ambient Organic Aerosols with High-Resolution Time-of-Flight
777 Aerosol Mass Spectrometry. *Environ. Sci. Technol.* **2008**, *42* (12), 4478–4485 DOI:
778 10.1021/es703009q.
- 779 (83) Hinsberg, W. D.; Houle, F. A. Kinetiscope <http://www.hinsberg.net/kinetiscope/> (accessed
780 May 1, 2019).
781



b) Squalane ($C_{30}H_{62}$)

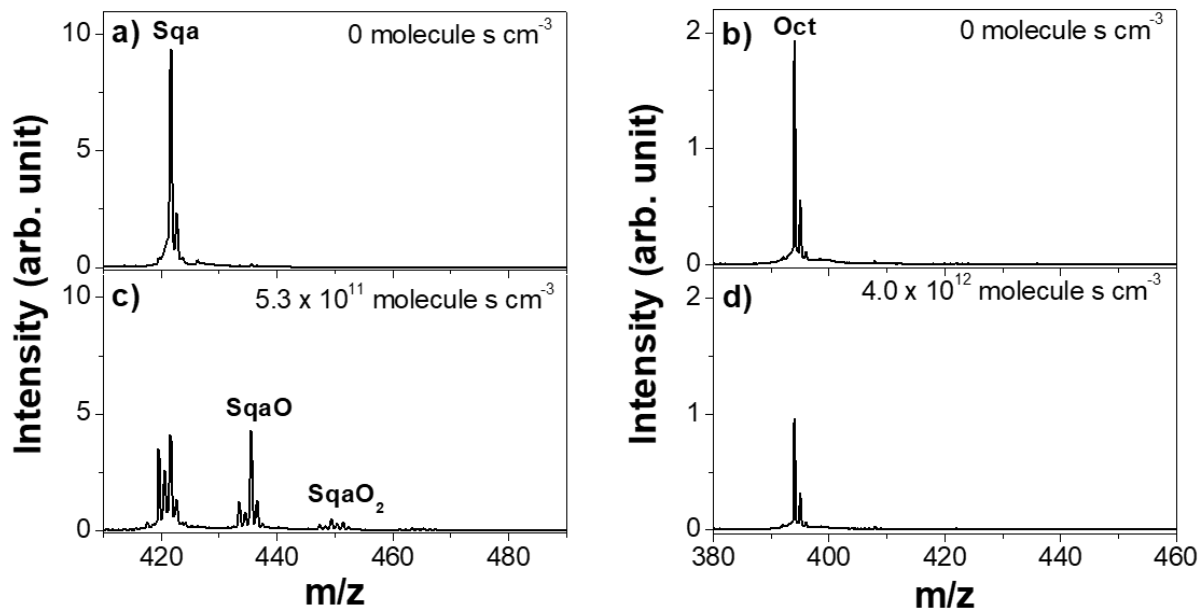


c) Octacosane ($C_{28}H_{58}$)

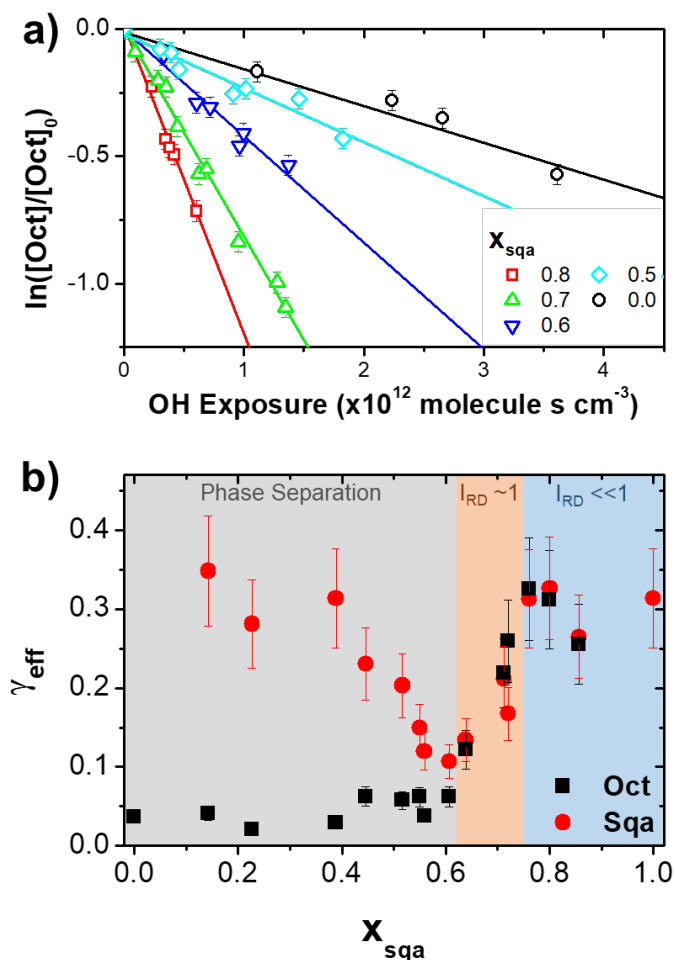


782
783
784
785
786
787

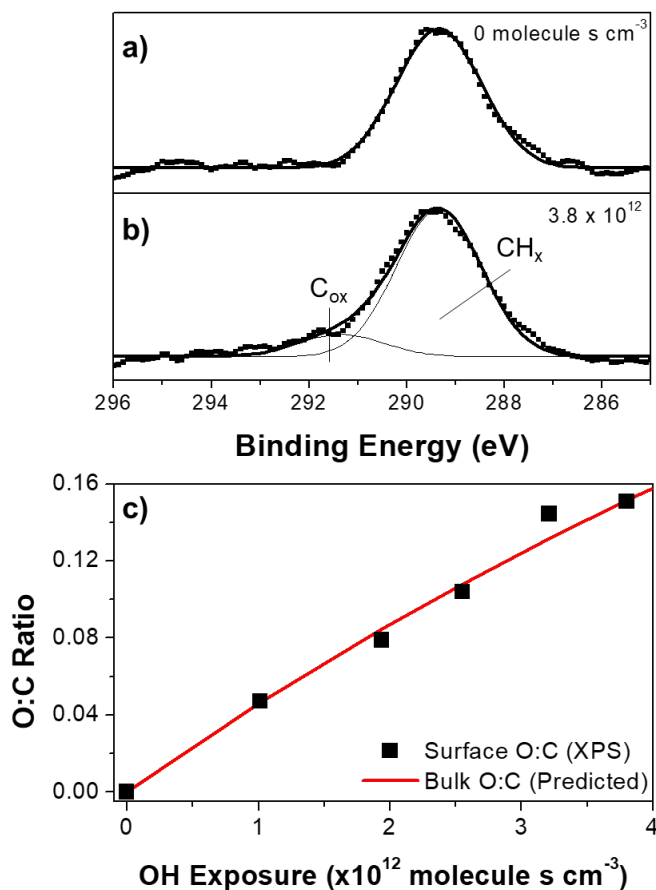
Figure 1. a) Schematic of flow tube setup (GC = Gas Chromatograph, SMPS = Scanning Mobility Particle Sizer, AMS = VUV Aerosol Mass Spectrometer, VMI = Velocity Map Imaging spectrometer). The chemical structures of squalane (b) and octacosane (c).



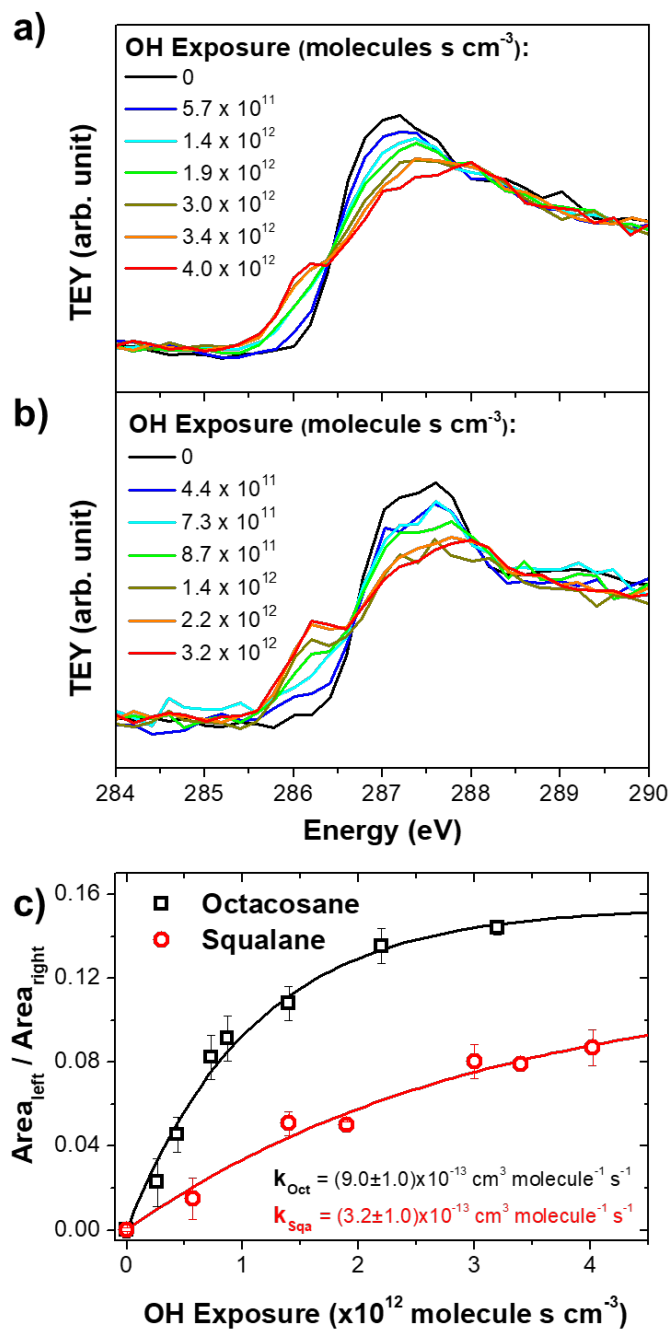
788
 789 **Figure 2.** a) Aerosol mass spectrum of squalane particles without exposure to OH radicals. The
 790 molecular ion is labeled as “Sqa”. b) The mass spectrum of octacosane particles without
 791 exposure to OH radicals. The molecular ion is labeled as “Oct”. c) The mass spectrum when
 792 about half of the squalane has reacted. Functionalized products with increasing numbers of
 793 oxygen (SqaO and SqaO₂) are present. d) The mass spectrum when about half of the octacosane
 794 has reacted. No products are observed when octacosane heterogeneously reacts.
 795



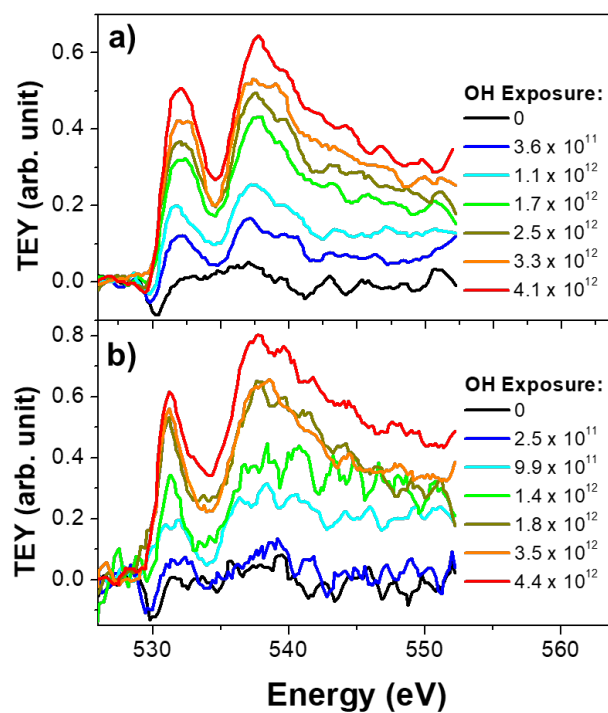
796
 797 **Figure 3.** a) Decay of the molecular ion of octacosane from heterogeneous oxidation in mixed
 798 octacosane-squalane particles with different compositions. b) Calculated effective uptake
 799 coefficients of octacosane and squalane in mixtures of the two. The blue shaded region
 800 represents compositions where reaction rate is OH flux limited ($I_{\text{RD}} \ll 1$). The orange shaded
 801 region represents compositions where diffusion limitations start to arise ($I_{\text{RD}} \sim 1$). The grey
 802 shaded region represents compositions where the particles are phase-separated.
 803



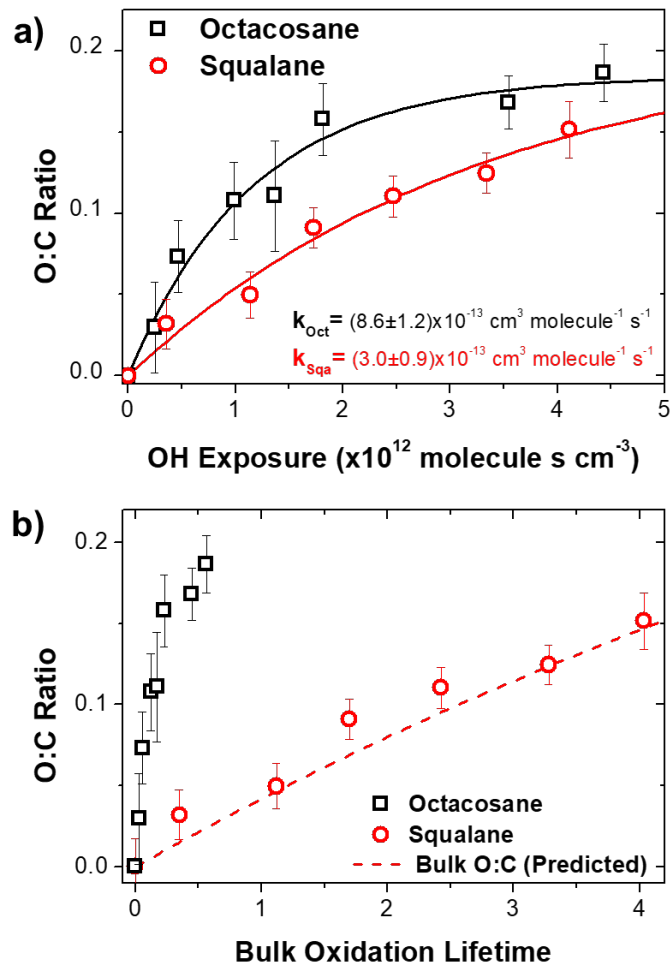
804
 805 **Figure 4.** a) and b) show the XPS spectrum of squalane particles oxidized at an OH exposure of 0
 806 and 3.8×10^{12} molecule s cm⁻³, respectively. Spectra were collected using 330 eV photons. c) The
 807 measured O:C ratio at the surface of squalane at different OH exposures. Only one oxygen atom
 808 is associated with each C_{ox} (i.e. only ketones and alcohols formed). The O:C ratio of the bulk was
 809 predicted using kinetics measured in previous work.⁷⁰



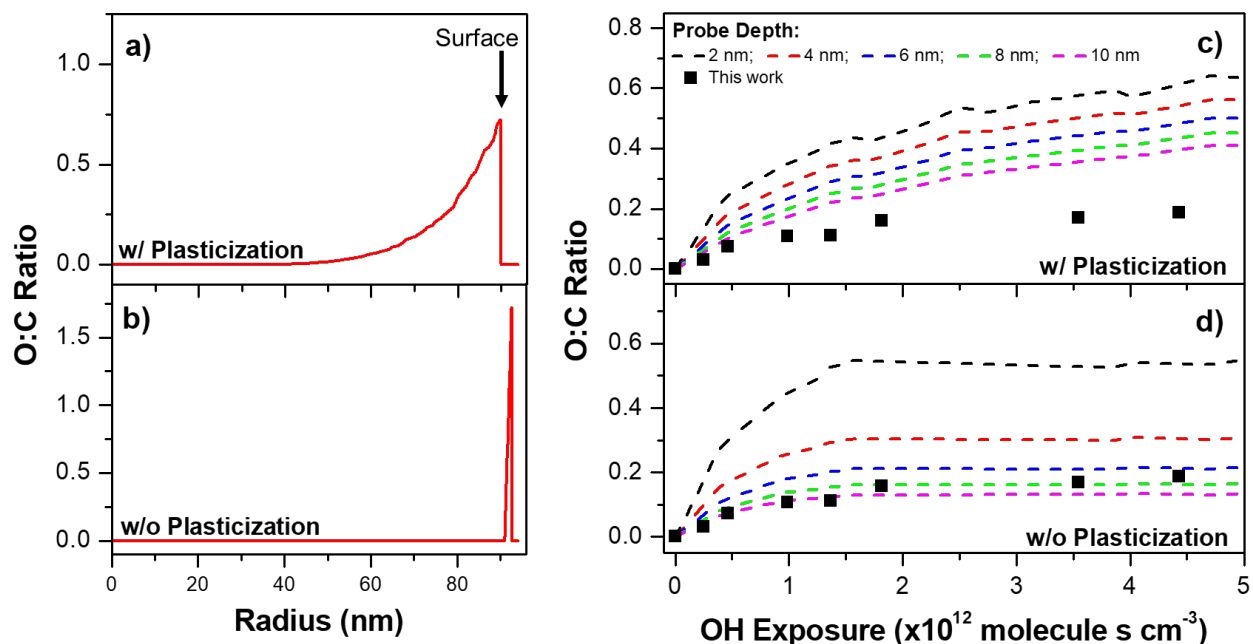
810
 811 **Figure 5.** Carbon K edge XAS spectra of squalane (a) and octacosane (b) particles at different OH
 812 exposures. Spectra were area normalized using the measured TEY intensity from 286-300 eV. c)
 813 Oxidation kinetics from carbon K edge XAS spectra were extracted by calculating the ratio of the
 814 area left of the isosbestic point (286.5 eV) to that right of the isosbestic point and plotting it as a
 815 function of OH exposure.
 816



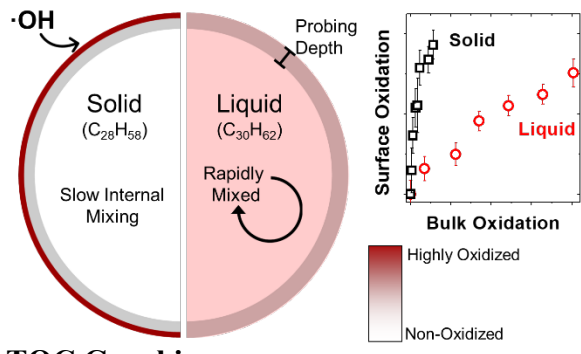
817
 818 **Figure 6.** Oxygen K edge XAS spectra of squalane (a) and octacosane (b) particles at different
 819 OH exposures. Spectra were normalized to the pre-edge intensity (526-528 eV).
 820



821
 822 **Figure 7.** a) Measured surface O:C ratio for squalane particles (red circles) and octacosane
 823 particles (black squares) at different OH exposures. The data were fit to Eq. 2 to determine the rate
 824 of change and the maximum O:C ratio. b) Measured surface O:C ratio for squalane and octacosane
 825 particles at different bulk oxidation lifetimes. Bulk oxidation lifetime was calculated using the bulk
 826 AMS measurements and Eq. 3. The dashed red line shows the bulk O:C ratio predicted for squalane
 827 from previous AMS measurements.⁷⁰
 828



829
 830 **Figure 8.** a,b) The internal distribution of the O:C ratio for triacontane particle with an initial
 831 radius of 190 nm after it has been heterogeneously oxidized at an OH exposure of 5.0×10^{12}
 832 molecule s cm^{-3} . The distribution from the model that includes plasticization is shown in (a). The
 833 distribution from the model that keeps diffusion constant is shown in (b). c,d) Estimates of the O:C
 834 ratio that would be measured with different probe depths (as determined by electron attenuation
 835 lengths). The experimental surface O:C ratios are overlaid (black squares). The changing surface
 836 composition with the plasticization model is shown in c), and the changing surface composition
 837 with the constant diffusion model is shown in d).
 838



839
840 **TOC Graphic**